Amorphous Calcium Phosphate Nanoparticles Allow Fingerprint Detection via Self-Activated Luminescence

Thales R. Machado,[a,b,*] Jussara S. da Silva,[b] Renata R. Miranda,[a] Valtencir Zucolotto,[a] Máximo S. Li,[c] Maria V.M. de Yuso,[d] Juan J. Guerrero-González,[e] Ieda L.V. Rosa,[b] Manuel Algarra,[f,g,*] Elson Longo[b]

[a] GNANO - Nanomedicine and Nanotoxicology Group, Physics Institute of São Carlos, University of São Paulo, 13566-590 São Carlos, SP, Brazil.

[b] CDMF - Center for the Development of Functional Materials, Federal University of São Carlos, 13565-905 São Carlos, SP, Brazil.

[c] Physics Institute of São Carlos, University of São Paulo, São Carlos, SP, Brazil.

[d] X-Ray Photoelectron Spectroscopy Lab. Central Service to Support Research Building (SCAI). University of Málaga. 29071 Málaga, Spain

[e] Policía Científica, Cuerpo Nacional de Policía, Málaga, Spain.

[f] Departamento de Ciencias, Universidad Pública de Navarra, Campus de Arrosadia, 31006 Pamplona, Spain.

[g] INAMAT^2-Institute for Advanced Materials and Mathematics, Campus de Arrosadia 31006 Pamplona, Spain.

*Corresponding authors

E-mail: tmachado.quimica@gmail.com (T.R. Machado)
malgarra67@gmail.com (M. Algarra)

ABSTRACT

In this work, stable activators-free photoluminescent nanoparticles based on amorphous calcium phosphate (ACP) were obtained for the first time, and their performance for latent fingerprint imaging was investigated. ACP nanoparticles with irregular rounded shape and diameters sized 10-40 nm were prepared by a rapid and simple chemical precipitation, followed by heat treatment at 400 ºC for 4 hours. Diffuse reflectance spectroscopy, photoluminescence excitation and emission measurements revealed a high density of localized energy states within the band gap of heat-treated ACP (E_g = 5.25-5.42 eV). This behavior allowed the excitation of ACP in the near-ultraviolet region (λ_{exc} = 450 nm, 2.75 eV), leading to an intense defect-related broadband (490-890 nm) photoluminescence emission centered at 540 nm (2.30 eV), which was 50 times more intense than that of untreated nanoparticles. The effect of both lattice shrinkage due to structural water elimination and the presence of vacancies (V_{Ca} and V_O in PO^{3-}_4) and carbonates (CO^{2-}_3) on the luminescent properties of ACP was discussed in detail and investigated after aqueous-mediated ACP crystallization into hydroxyapatite (HA). ACP nanoparticles were found to be non-cytotoxic, as determined by MTT assay using HDFn cell line, reaching cell viabilities superior to 95% in all tested concentrations (20-320 μg/mL) after an incubation period of 24 and 48 hours. Fingerprint images were obtained using ACP nanoparticles under near-ultraviolet irradiation (λ_{exc} = 450 nm) on tweezers and the LCD screen of a smartphone, and then successfully validated by the Integrated Automated Fingerprint Identification System used by the Scientific Police in Spain. The present results evidenced that the new luminescent ACP nanoparticles are safe to be used and agree with the forensic requirements for future legal actions.

Keywords: Calcium phosphate; Nanoparticles; Luminescence; Defects; Forensics; Fingerprint Imaging

1. Introduction

Fingerprint analysis is one of the most explored biometric recognition approaches in forensic science for personal identification [1,2]. Usually, fingerprints left on surfaces cannot be observed by the naked eyes, often requiring a post-processing step, such as powder dusting, chemical fuming, and through typical formulations based on organic and fluorescent dyes [3–8]. Remarkably, since the pioneering use of zinc sulfide phosphor (ZnS) [9], photoluminescent powders have been the most requested approach due to their resistance to photobleaching and the ability to produce high-resolution and sensitive fingermarks when illuminated by ultraviolet (UV) radiation.

Up to now, a variety of strategies based on nanotechnology has focused on the improvement of the fluorescence intensity and stability of distinct materials in order to obtain fluorescent images of fingerprints with higher contrast. Many studies have investigated colloidal semiconductors, such as quantum dots, whose main properties are strongly based on their particle size [10–15]; rare earth nanoparticles (NPs), whose increase in the emission quantum yield can be assigned to *f* transitions in the shell environment [16–18]; and noble metal NPs, whose importance can be attributed to their inert nature [19–22]. Recently, carbon NPs and carbon dots have emerged as potential candidates for application as fluorescent NPs [23–27].

Specifically, luminescent NPs comprised of the calcium orthophosphate (CaP) family are interesting for forensic purposes, mainly due to their superior biodegradability, biocompatibility and easily scalable synthetic routes [28,29]. However, current research based on luminescent CaPs NPs, mostly focused on hydroxyapatite (HA) and amorphous calcium phosphates (ACPs), has pointed towards other technological fields such as nanomedicine [30]. The prominence of these NPs can be associated with their high capacity to incorporate foreign ions, for example, lanthanide ions, thus improving their luminescent properties [31].

On the other hand, Zollfrank et al. [32] and Aronov et al. [33,34] demonstrated the occurrence of intrinsic photoluminescence (PL) in HA and attributed this behavior to the presence of defect-

related localized energy states. Since then, self-activated luminescence mechanisms in HA micro- and nanoparticles have been studied by several research groups [35–43] and optimized for monitored drug delivery [44–48], bioimaging [49–51], biosensing [52,53], and secure information storage [54]. The main advantage of these strategies is that HA is constituted by earth-abundant and relatively low-cost elements, where the achievement of intense luminescence avoids the need of doping with activator species. Also, the intrinsic luminescence was employed as a method to characterize HA-based photocatalysts [55], structural and compositional changes in bones [56,57], and early caries detection [58].

In this study, the correlation among structural, optical and PL properties of ACP NPs was investigated for the first time and compared with those of HA NPs. ACP has significant structural resemblances with HA and is the first CaP phase precipitated from supersaturated aqueous solutions at the initial stages of the reaction between calcium and phosphate ions [59]. Therefore, ACP can be prepared by faster and easier synthetic routes, such as chemical precipitation. However, special attention is necessary to avoid its spontaneous crystallization into other CaPs. Herein, ACP NPs were washed and recovered 1 min after precipitation. The post-heat treatment step conducted at 400 ºC plays two important roles: first, to increase the ACP phase stability, a well-known strategy to obtain stable powders at room temperature [60]; and second, to improve the luminescent properties of ACP NPs, a crucial step observed for other CaPs [37,50]. Based on these results, this study allows the obtention of non-toxic and stable luminescent ACP NPs that can be used for the sensitive development of latent fingerprints.

2. Materials and methods

2.1. Materials

Calcium nitrate tetrahydrate ($Ca(NO_3)_2.4H_2O$, 99%) and di-ammonium phosphate ($(NH_4)_2HPO_4$, 98+%) were purchased from Sigma-Aldrich and Strem Chemicals, respectively. Ammonium

hydroxide, absolute ethanol, and acetone were acquired from Labsynth. Human Dermal Fibroblast neonatal (HDFn, catalog number C0045C) cell line was provided by Thermo Fischer Scientific. Dulbecco's Modified Eagle Medium (DMEM) and Fetal Bovine Serum (FBS) were purchased from Vitrocell. MTT (3-[4,5-dimethylthiazol-2-yl]-2,5-diphenyltetrazolium bromide) and dimethyl sulfoxide (DMSO) were acquired from Sigma-Aldrich and Labsynth, respectively. All reagents were used as received without further purification.

2.2. Synthesis

The amorphous calcium phosphate (ACP) NPs were synthesized via an easy approach based on chemical precipitation. First, 50 mL of an aqueous phosphate solution (6 mmol of $(NH_4)_2HPO_4$, pH ~ 8.5) and 100 mL of an aqueous calcium solution (10 mmol, $Ca(NO_3)_2.4H_2O$, pH ~ 6.8) were placed in separate flasks under vigorous stirring at room temperature. The pH values of both solutions were adjusted to ~10 by adding ammonium hydroxide. Then, the phosphate solution was added to calcium solution by one-batch step, and the resulting mixture was stirred for 1 min. The solid product was recovered and washed thoroughly by centrifugation with water and acetone. The resulting slurry was dried at 60 ºC for 4 h in air (referred to as ACP sample). Then, the ACP powder was placed in alumina crucible and heat-treated at 400 ºC/4h in a programmable furnace at a heating rate of 10 ºC/min. The sample was then naturally cooled down to room temperature (referred to as ACP400 sample). Comparatively, we also allowed the crystallization of ACP in the HA structure by increasing the aging step from 1 min to 24 h for a fraction of the resulting calcium and phosphate mixed solution described above. In this case, the solid product was recovered and washed several times with water and ethanol by centrifugation and dried overnight at 80 ºC. The HA sample was heat-treated at 400 ºC/4h in the same conditions as those used for the ACP powder (referred to as HA400 sample).

2.3. Characterization

Transmission electron microscopy (TEM) was performed on a FEI TECNAI F20 (Netherlands) microscope operating at 200 kV. The as-prepared samples were structurally characterized by X-ray diffraction (XRD) on a Shimadzu (Japan) XRD-6000 diffractometer using CuK_α radiation (λ = 0.154184 nm). The data were collected at a step scan rate and step size of 0.2°/min and 0.02°, respectively. Fourier transform infrared (FTIR) spectroscopy was carried out using a Thermo Scientific (USA) Nicolet iS50 spectrometer operating in absorbance mode. The spectra were recorded at a resolution of 4 cm^{-1} over a wavenumber range of 400-4000 cm^{-1}. The peak asymmetry (ΔS) was estimated according to Equation 1 [61,62]:

$$\Delta S = (H_R - H_L)/(H_R + H_L) \quad (1)$$

where H_R and H_L are the right and left components of the full width at half maximum (FWHM) of the v_3PO_4 and v_4PO_4 bands, respectively.

X-ray photoelectron spectroscopy (XPS) studies were performed on a Physical Electronics PHI (USA) VersaProbe II spectrometer using monochromatic Al-K_α radiation (49.1 W, 15 kV and 1486.6 eV) in order to analyze the core-level signals of the elements of interest with a hemispherical multichannel detector. The sample spectra were recorded with a constant pass energy value of 29.35 eV using a 200-µm diameter circular analysis area. The XPS spectra obtained were analyzed with the aid of PHI SmartSoft software and processed using MultiPak 9.3 package. The binding energy values were referenced to adventitious carbon C 1*s* signal (284.8 eV). Shirley-type background and Gauss-Lorentz curves were used to determine the binding energies. Ultraviolet-visible (UV-Vis) spectroscopy was performed on a Shimadzu UV-2600 (Japan) spectrophotometer operating in diffuse reflectance mode. Excitation and emission PL spectra were acquired on a Horiba Jobin Yvon (Japan) spectrofluorometer model Fluorolog-3, equipped with a 450 W Xe lamp as the excitation source. Signals were collected by a visible photodiode detector model PPD-850 (Japan). All spectra were corrected by the lamp profile and detector response. PL spectroscopy was also conducted at room

temperature using a Kimmon Koha (Japan) IK5451R-E HeCd laser (λ_{exc} = 450 nm) and a Coherent (USA) Innova 200 K krypton laser (λ_{exc} = 405 nm) as the excitation sources.

2.4. Cytotoxicity assay

HDFn cells were employed to investigate the potential cytotoxicity of ACP400 NPs in order to probe if they were safe to be used for forensics purposes. The cells were cultured as a monolayer in DMEM supplemented with 10% v/v inactivated FBS at 37 °C and 5% CO_2. For the cell viability analysis, the cells were seeded onto a 96-well microplate at 2×10^4 cell/mL. After 24 h, the medium was replaced with fresh complete medium containing the NPs at different concentrations (0, 20, 40, 80, 160 and 320 μg/mL) and the cells were incubated for 24 and 48 h. At the end of the exposure periods, the HDFn cells were incubated with 0.5 mg/mL of MTT for 2 h and washed with phosphate-buffered saline, followed by formazan solubilization with 200 μL of DMSO. The absorbance was recorded at 570 nm using a Molecular Devices (USA) SpectraMax M3 plate reader. Three independent experiments with three replicates each were conducted. Data distribution was tested, and one-way analysis of variance (ANOVA) tests were performed, followed by Dunnett's post-test. Cytotoxicity was investigated by the comparison between control and groups containing the NPs. *p*-values smaller than 0.05 were considered to be statistically significant.

2.5. Fingerprint imaging

The recorded fingerprints were validated by the IAFIS (3M Cogent's Integrated Automated Fingerprint and Identification System), a customizable software package that allows to perform a wide range of tasks for processing, editing, searching, retrieving, and storing fingerprint images and subject records used by the Scientific Police in Spain. The acquisitions of the fluorescent fingerprints on the different surfaces were conducted by a Rofin (Australia) Polilight PL10. Excitation bands in the NUV region (λ_{exc} = 350 and 450 nm) were used with yellow goggles (495 nm, edge wavelength) and orange goggles (edge wavelength 550 nm), respectively. The 450-nm excitation conditions produced superior

images and further work was confined to this wavelength. The images of latent fingerprints were obtained using a Nikon (Japan) Multi-zoom AZ-100 microscope and Digital Sight-5Mc connected to the microscope by a computer, in which the pictures were stored and visualized by NIS-Elements software. The microscope was equipped with an epifluorescence system containing a mercury lamp (100 W) for sample illumination and a variety of available filter blocks (UV-2A: EX 330-380; DM 400; BA 420).

3. Results and discussion

3.1. Morphology and long-range order (LRO) analysis

The morphological aspects of the as-prepared ACP and ACP400 samples were investigated by TEM, and the obtained images are displayed in Figures 1a and 1b, respectively. Both samples are composed of chain-like NPs with irregular rounded shape and diameters ranging mainly from 10 to 40 nm. No significant difference in the morphological aspects was observed between the samples. The selected area electron diffraction (SAED) pattern of the ACP400 NPs shows a typical pattern of an amorphous material (inset in Figure 1b). The chemical composition of this sample was evaluated by energy-dispersive X-ray spectroscopy (EDS) (Figure 1c), indicating the presence of the elements Ca, P, and O, which represent the main constituents of the ACP structure. The presence of C can be attributed to the carbon film of the TEM grid.

Figure 1d displays the XRD patterns of the ACP sample precipitated at room temperature, where no discernible peaks of crystalline CaP phases can be observed. Instead, the broad diffraction halo at $2\theta = 30°$ indicates that an amorphous phase with lack of LRO was preserved [63]. A poorly crystallized phase appears when the reaction time is increased to 24 h (Figure S1a). This can be attributed to the spontaneous conversion of ACP into calcium-deficient HA ($Ca_{10-\times}(HPO_4)_\times(PO_4)_{6-\times}(OH)_{2-\times}$ ($0 < \times < 1$)) in the mother solution [59]. As also shown in Figure 1d, the amorphous pattern of the ACP sample persists after heat treatment at 400 ºC for 4 h (ACP400 sample), demonstrating the thermal stability of this amorphous phase. The thermally induced

crystallization of the ACP sample is only observed under annealing at higher temperatures (600 ºC/4h), where peaks corresponding to the monoclinic α-tricalcium phosphate (α-TCP, α-$Ca_3(PO_4)_2$) phase are discernible (Figure S2). ACP is known to assume a hydrated TCP-like structure and stoichiometry ($Ca_3(PO_4)_2$) with the experimental conditions adopted [62,64], and posterior annealing procedures (T ≥ 600 ºC) tend to lead to a solid-state reordering of ACP in the crystalline TCP phases [65].

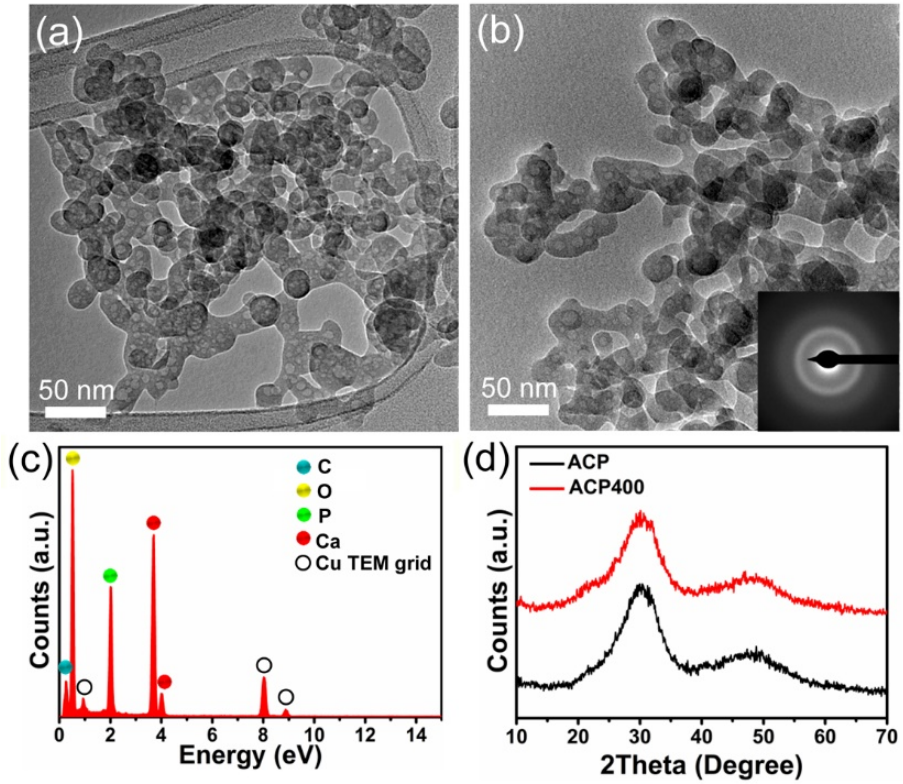

Figure 1. TEM micrographs corresponding to (**a**) ACP and (**b**) ACP400 NPs (SAED pattern, inset), (**c**) EDS elemental analysis of ACP400 NPs, and (**d**) XRD patterns of the prepared samples.

3.2. Short-range order (SRO) analysis

Figure 2a shows the FTIR spectra of ACP and ACP400 samples. The main vibrational modes of the PO_4^{3-} groups, including the asymmetric stretching mode of P–O bond (ν_3) in the 1300-900 cm^{-1} range and the symmetric stretching mode of P–O bond (ν_1) appearing as a shoulder, as well as the bending mode of O–P–O bond (ν_4) in the 685-485 cm^{-1} range, can be clearly seen [66]. The broad and unsplit ν_3 and ν_4 modes observed are characteristic of the ACP phase [67,68]. The presence of these

vibrational bands evidences a certain degree of SRO of the atomic groups in the ACP and ACP400 NPs despite the lack of structural LRO detected by XRD. The doublet between 1600-1375 cm^{-1} is assigned to the asymmetric stretching mode of C–O bond (ν_3) of the CO_3^{2-} group, whereas the low intensity band centered at 871 cm^{-1} is related to the bending mode of O–C–O bond (ν_2) of this same group [66]. The presence of CO_3^{2-} impurity is typically associated with the precipitation of ACP under atmospheric conditions, which causes the solubilization of CO_2 from air, followed by the slight incorporation of the resulting CO_3^{2-} groups into the amorphous material [69]. Lastly, the bands associated with the vibrational modes of water molecules are observed in the range between 3700-2500 cm^{-1} and at 1655 cm^{-1} [70].

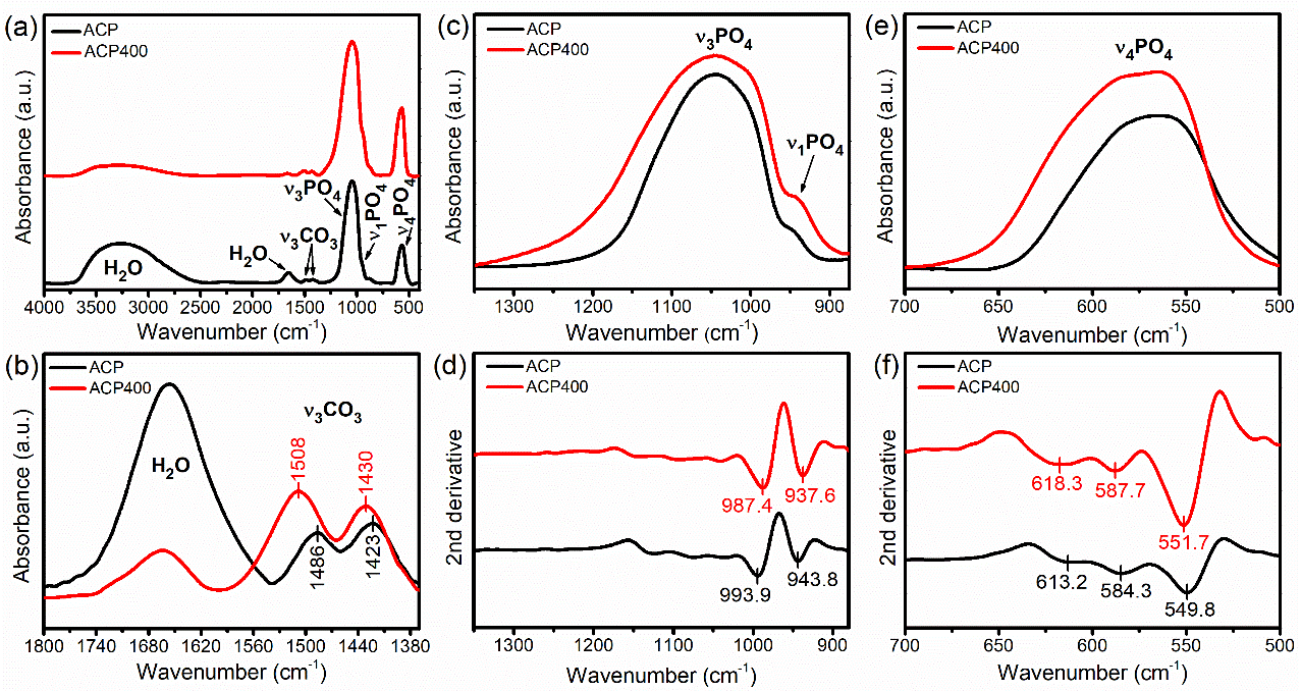

Figure 2. (a) FTIR spectra of ACP and ACP400 samples, **(b)** magnified view of H_2O and ν_3CO_3 bands, **(c,e)** magnified views of ν_3/ν_1PO_4 and ν_4PO_4 bands, respectively, and **(d,f)** 2nd derivative spectra of ν_3/ν_1PO_4 and ν_4PO_4 bands, respectively.

According to Figures 2a and 2b, there is a remarkable difference in the FTIR spectra between the ACP and ACP400 NPs regarding the intensity of H_2O bands, which significantly decreases in the latter sample. Eanes [65] demonstrated that chemically precipitated ACP obtained at similar alkaline

conditions (pH = 9.5-10) can retain ~15 wt% of water even after lyophilization, leading to almost three water molecules per formula unit, i.e., $Ca_3(PO_4)_2.3H_2O$ stoichiometry. Holmes and Beebe [71] concluded that ~25% of this value corresponds to adsorbed water, whereas ~75% are tightly bounded water molecules inside the ACP structure. More recently, Uskoković et al. [62] corroborated these seminal studies by obtaining similar water contents of 16.8 wt%, of which 30% are adsorbed on the ACP surface and 70% are inside the solid framework. Therefore, the dehydration observed in the ACP400 sample is mainly associated with the irreversible elimination of these water molecules inside the ACP structure that occurs in the 25-400 ºC temperature range and, to a lesser extent, with the reversible loss of adsorbed water [60,62,71].

According to Figures 2c and 2e, there is a broadening in the PO_4^{3-} bands related to internal, short-range ν_3 and ν_4 vibrational modes when the ACP NPs are heat-treated at 400 ºC, causing an increase in the FWHM values from 150 and 77 cm^{-1} for ACP NPs to 190 and 90 cm^{-1} for ACP400 NPs, respectively. These values represent a FWHM increase of 27% (ν_3) and 17% (ν_4) in ACP400. Moreover, the ν_3 and ν_4 bands of the PO_4^{3-} groups become more asymmetrical in shape due to the heating procedure, leading to a peak asymmetry (ΔS) of 0.14 and 0.16 for ACP NPs to 0.21 and 0.23 for ACP400 NPs, which means a ΔS increase of 50% and 44%, respectively, for these bands. As stated by Uskoković [61], these data can be interpreted as a decrease in SRO in the PO_4^{3-} groups of ACP400 NPs, with a consequent larger absorption of varied frequencies – although temperature-related structural changes usually tend to lead to higher degrees of structural order in materials. As previously discussed, an important loss of tightly bounded water occurred in ACP400 (Figures 2a and 2b). This liberation is known to cause an overall contraction in the ACP lattice, thus removing empty spaces [61]. As a consequence, the structural shrinkage significantly increases the lattice strain and leads to even more distorted environments around the PO_4^{3-} clusters, provoking the asymmetric broadening of

v_3 and $v_4PO_4^{3-}$ modes due to fluctuations in P–O bond lengths and O–P–O bond angles inside the PO_4^{3-} structure.

Some further evidences of structural changes in the PO_4^{3-} groups and their neighborhoods by annealing at 400 ºC are the redshift of one observable component of the triply degenerated asymmetric stretching mode (v_3) from 994 to 988 cm^{-1}, the redshift of the non-degenerated symmetric stretching mode (v_1) from 943 to 937 cm^{-1} and, in contrast, the blueshift of all components of the triply degenerated bending mode (v_4) from 612, 585, 550 to 618, 588, 553 cm^{-1}, respectively, as analyzed by the second-derivative plots (Figures 2d and 2f). This effect is associated with stronger interactions between the PO_4^{3-} groups and the near-neighbor atoms in the ACP shrunk lattice that occurs at temperatures below the amorphous-to-crystalline phase transition [61].

In the v_3 bands of the CO_3^{2-} groups (Figure 2b), important features are sensed after the heat treatment procedure: (**i**) a blueshift of the doublet from 1486 and 1422 cm^{-1} to 1507 and 1431 cm^{-1}, and (**ii**) a slight increased separation of the doublet from 64 to 76 cm^{-1}. These characteristics of the v_3 modes are sensitive to the structural location of CO_3^{2-} impurities in CaPs [72] and susceptible to changes in the amount of hydration water within the lattices with surroundings that strongly interact with these groups [73–76]. In this sense, the present results indicate that the CO_3^{2-} groups are influenced by the compositional and organizational changes in the surroundings due to water loss and lattice contraction, leading to different stereochemistry for the CO_3^{2-} groups with more energetic C–O bonds.

3.3. Surface analysis

The surface chemical composition of the ACP400 sample is based on O 1*s* (53.9 at.%), C 1*s* (17.2 at.%), P 2*p* (12.8 at.%) and Ca 2*p* (16.1 at.%), as detected by the survey scan (Figure 3a). Basically, the XPS analysis showed that the most important information was found in the C 1*s* signal (Figure 3b), which can be deconvoluted into three main contributions. The main peak at 284.8 eV is

attributed to graphitized carbon after heat treatment at 400 ºC (C–C/C–H bonds), while the other two shoulders at 286.8 and 289.1 eV are assigned to C–O and C=O (carbonyl)/O=C–O$^-$ (carboxyl) bonds, respectively, which are assigned to CO_3^{2-} on the surface of ACP400 NPs [77]. Moreover, O 1*s* was deconvoluted into three main contributions at 531.0 (C=O), 533.1 (C–O/P=O) and 534.7 eV (P–O) [78] (Figure 3c). These results confirm the presence of graphitized carbon and CO_3^{2-} groups from ACP. The other peaks related to P 2*p* do not reveal relevant inputs. The signal attributed to the PO_4^{3-} component reveals a single peak, indicating that all P atoms have equivalent environment.

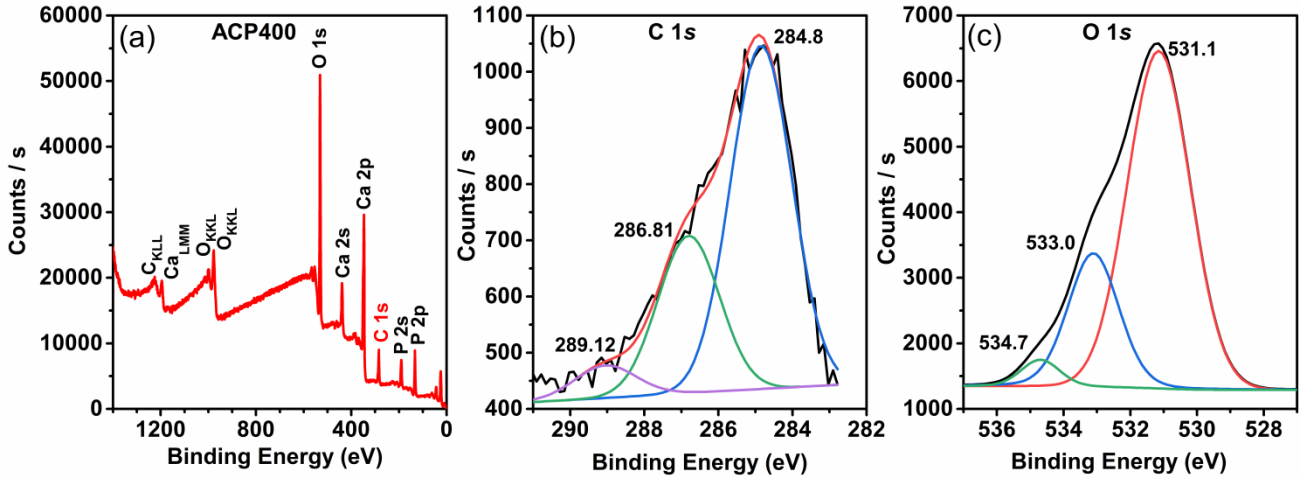

Figure 3. (**a**) Survey XPS spectrum of ACP400 NPs. High-resolution XPS spectra of (**b**) C 1*s* and (**c**) O 1*s*.

3.4. Optical properties

In a semiconductor, the optical band gap energy (E_g) describes the energy needed to excite an electron from the valence band (BV) to the conduction band (CB). E_g can be estimated by the Tauc's method according to Equation 2:

$$(\alpha h\nu)^{1/n} = A(h\nu - E_g) \qquad (2)$$

where α is the absorption coefficient, hν is the incident photon energy, A is a constant depending on the transition probability, and n is equal to 1/2 or 2 for direct and indirect transition band gaps, respectively [79]. Diffuse reflectance spectroscopy is often used to determine the E_g value. Figure S3

displays the reflectance spectra obtained for the ACP and ACP400 samples. The Kulbelka-Munk function, $F(R_\infty)$, can be derived from these spectra as given by Equation 3:

$$F(R_\infty) = \frac{(1 - R_\infty)^2}{2R_\infty} = \frac{\alpha}{s} \qquad (3)$$

where R_∞ is the reflectance and *s* is the scattering coefficient. $F(R_\infty)$ is proportional to α, assuming that *s* is wavelength-independent and can substitute α in Equation 3 [80]. The plot of $[F(R_\infty)h\nu]^{1/n}$ vs. hν leads to the Tauc plot, and the E_g value is obtained by fitting and extrapolating the linear portion of the plot to the energy axis. Figures 4a and 4b show the Tauc plots of our samples considering the previous approach. Additionally, we also used a linear fit as the abscissa (blue dotted line) for each spectrum with significant sub-bandgap absorption. According to Makuła et al. [81], the use of this baseline method leads to a more accurate estimation of the E_g value by the intersection of the two fitted lines.

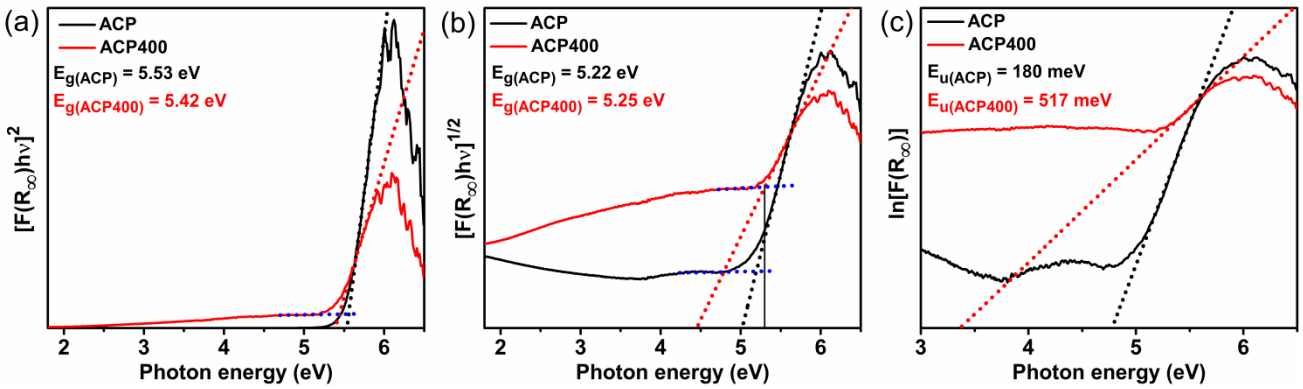

Figure 4. E_g and E_u energies for ACP and ACP400 samples. Tauc plots for (**a**) direct transition (n = 1/2) and (**b**) indirect transition (n = 2). (**c**) Plots of $\ln[F(R_\infty)]$ *vs.* photon energy.

Two important insights can be extracted from the results. First, the E_g values calculated for both ACP (E_g = 5.53 and 5.42 eV for n = 1/2 and 2, respectively) and ACP400 samples (E_g = 5.22 and 5.25 eV for n = 1/2 and 2, respectively) are closely related to those found in crystalline CaPs, including α-TCP (E_g = 4.89 eV) and β-TCP (E_g = 5.25 eV) [82], with direct band gap transitions, as well as HA (E_g = 4.51─5.78 eV) [37,83–87] and Ca-dHA (E_g = 5.67 eV) [88], with indirect band gap transitions. The band structures of these materials are mainly composed of overlapped P 3*s,* P 3*p* and O 2*p* orbitals

from covalent PO_4^{3-} groups at the upper VB, with minor contributions of Ca 4*s* and 3*d* components due to ionic interactions between Ca and O from neighboring PO_4^{3-} groups as well as components from OH groups (in the case of HA and Ca-dHA), whereas the bottom of the CB is mainly formed by Ca 3*d* components [82–85,88]. Since SRO is the key feature for the electronic properties of a solid [79], we can assume that the close E_g values between our ACP samples and those found for other CaPs emerge from the structural similarities at short range between the amorphous and crystalline phases, leading to comparable band structures.

Second, a decrease in E_g from 5.53 to 5.42 eV (Figure 4a) is observed when the heat treatment is performed at 400 ºC/4h. This decrease is accompanied by an increment in tailing of band states which extend within the forbidden gap. In poorly crystalline and amorphous materials, the presence of these tails of energy states instead of sharp band edge absorptions is characteristic of a broad distribution of defect levels, which vary according to the degree of lattice disorder [89]. The tail absorption exponentially depends on photon energy, and the plot of $\ln[F(R_\infty)]$ vs. hν can be used to calculate the Urbach energy (E_u) or Urbach tail width by the slope of the straight line obtained in this plot (in our case, E_u = 180 and 517 meV for ACP and ACP400, respectively, as shown in Figure 4c). The decrease in E_g and increase in E_u after the heat treatment step could be attributed to an increment in the lattice disorder (lower degree of SRO) for ACP400 compared to the ACP sample due to the wider deviations of bond lengths and bond angles from the ideal values, as also observed by FTIR data (section 3.2).

3.5. PL properties

Figures 5a and 5b show the excitation spectra of ACP and ACP400 NPs recorded by monitoring the main PL emission at λ_{em} = 530 and 540 nm, respectively. The broad and intense band centered at 243 nm (5.10 eV) observed in both samples can be attributed to the excitation departing from band states and localized tail states. The inset in each figure shows a magnified view over a selected wavelength region (260-520 nm). A weak but clear band extending up to 500 nm with maxima at 370 nm (3.35

eV) and 398 nm (3.12 eV) can be observed in ACP NPs. On the other hand, this same region in the ACP400 NPs is composed of a weak band in the 300-375 nm range with maximum at 317 nm (3.91 eV), as well as a band in the 400-520 nm range with maxima at 456 nm (2.72 eV) and 484 nm (2.56 eV). As the excitation energies are much lower than the E_g values in both samples, these bands can be assigned to the excitation involving localized energy states from point defects in the ACP structure, as already observed in other materials with similar spectral features [90]. These data evidence that there is an important reorganization of energy levels within the band gap in ACP when the thermal treatment is performed.

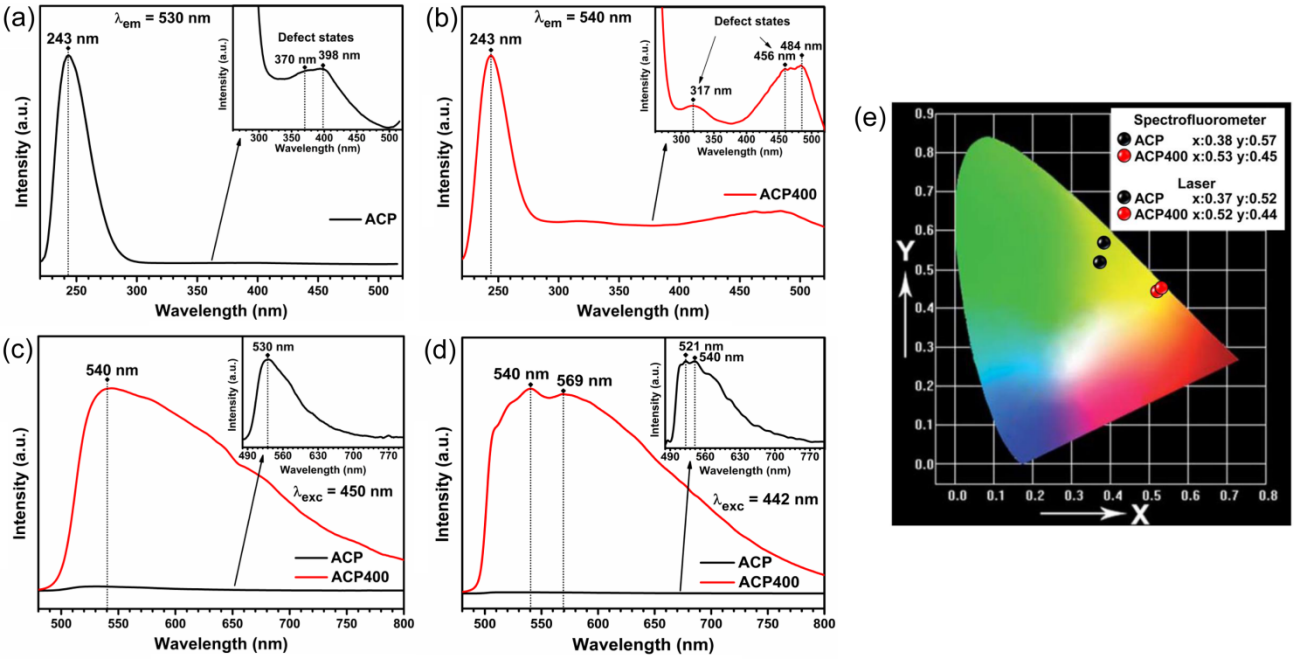

Figure 5. (a,b) PL excitation spectra of ACP and ACP NPs, respectively. PL emission spectra obtained by (c) a spectrofluorometer (λ_{exc} = 450 nm) and (d) an HeCd laser (λ_{exc} = 442 nm).

Figure 5c shows the PL emission spectra of ACP and ACP400 NPs recorded at λ_{exc} = 450 nm. This excitation wavelength was selected to resemble the one employed in fingerprint analysis. Both samples exhibit broadband emission profiles originated from radiative recombination of electron-hole pairs (e^-–h^+) through pathways that can encompass extended energy states as well as countless localized energy states. Considering that both the excitation and the emission wavelengths have

significantly lower energies than the calculated E_g, the contribution of band-to-band transitions between extended energy states is negligible. The emission band of ACP NPs ranges from 490 to 740 nm and reaches its maximum of intensity at 530 nm (2.34 eV), whereas for ACP400 NPs the emission band is broader and falls into the 490-800 nm range, with maximum at 540 nm (2.30 eV). Another remarkable feature observed in the PL spectra is the expressive increase in intensity by at least 50 times after heat treatment at 400 ºC.

To evaluate the effect of distinct excitation sources on the PL properties of the prepared samples, the emission spectra were also recorded using the 442 nm line of an HeCd laser (Figure 5d). Only a minor change in the inclination of the bands at shorter wavelengths was sensed due to the distinct configuration of the optical filters employed, together with a slight increase in the resolution of the emission bands when compared to the spectra acquired via spectrofluorometer, resulting in maxima centered at 521 and 540 nm for ACP NPs and at 540 and 569 nm for ACP400 NPs. This feature is mainly related to the narrower excitation line of the laser source.

The distinct characteristics observed between the emission profiles of ACP and ACP400 NPs (Figures 5c and 5d) influenced the color of the PL observed mainly because of the increase in the relative contribution of radiative emissions at longer wavelengths in the ACP400 sample. Figure 5e shows the Comission Internationale de l'Éclairage (CIE) chromaticity diagram. It is possible to note that the CIE coordinates shift from x = 0.38/0.37 and y = 0.57/0.52 for ACP to x = 0.53/0.52 and y = 0.45/0.44 for ACP400 (spectrofluorometer/laser), corresponding to green-yellow and yellow-orange regions, respectively. Additionally, the close-related CIE coordinates for both excitation sources confirm the reproducibility of the emission profiles using distinct luminescence techniques and indicate that the color of the PL observed was not considerably affected.

3.7. Hypotheses for PL properties of ACP

The nature of the PL properties in ACP is not completely clear yet, but according to this study the determining factor is the presence of localized energy states due to order-disorder effects. In the last years, the electronic structure and PL properties of HA have been studied because of its potential applications in optical devices and nanomedicine [30]. However, no previous literature has addressed the ACP structure. In this sense, to better elucidate the nature of PL emissions in the amorphous NPs, we measured the emission spectra of ACP after allowing its conversion into calcium-deficient HA, and the results are illustrated in Figures 6a-c. To this end, we excited our samples at λ_{exc} = 405 nm with a higher energy laser source to compare our results with those from previously published studies [37,40]. Interestingly, both amorphous (ACP) and poorly crystallized (HA) samples presented broadbands with comparable profiles. A plausible reason for the similar PL emission spectra after ACP→HA transition could be explained based on their structures at short range.

ACP NPs were found to exhibit SRO due to the presence of randomly packed $Ca_9(PO_4)_6$ units with an average size of 9.5 Å (Posner's clusters) [63], which in turn resemble a spatial subset of Ca^{2+} and $PO^{3}_{4}^{-}$ in the HA unit cell [59]. The mechanisms governing the ACP→HA transition are not yet fully understood, but it is well accepted that aqueous environments play a key role in the occurrence of solid-state reorganization, dissolution/reprecipitation, self-assembly aggregation and partial dissolution-aggregation mechanisms [91,92]. More to the point, several studies have experimentally confirmed the existence of the proposed Posner's clusters and the fact that these basic pre-nucleation clusters are conserved during ACP→HA transformation [92–94]. In other words, although there is a LRO increase in the ACP→HA phase transition with the presence of translational symmetry and stricter distribution of environments in the HA structure, both materials have similarities regarding the short- and medium-range spatial organization of atomic groups [59,61], which could result in comparable atomic interactions and electronic structures (see section 3.4), as also observed in other amorphous/crystalline semiconductors [79].

Considering the previous discussion, it is also plausible that the order-disorder effects that govern the PL for chemically precipitated ACP and HA samples have similar nature. Herein, the PL emission in the HA structure is probably due to perturbations of Ca and PO_4 electronic densities, which lead to new acceptor- and donor-like localized states inside the band gap [38]. These states arise from the VB and the CB, respectively, with Ca 3*p,* Ca 4*s*, P 3*s,* P 3*p*, O *2s* and O 2*p* characters [95]. This lattice disorder can be mainly attributed to ionic vacancies (V_{Ca}, V_H, V_{OH}, and V_O in the PO^{3-}_4 groups) and distortions in the bond lengths and bond angles of the structural coordination clusters [36,38,41,95,96]. Some reports also concluded that the CO_3^{2-} impurity and defects associated with its stabilization in the HA lattice could contribute to the defect-related PL emission [40,46,50].

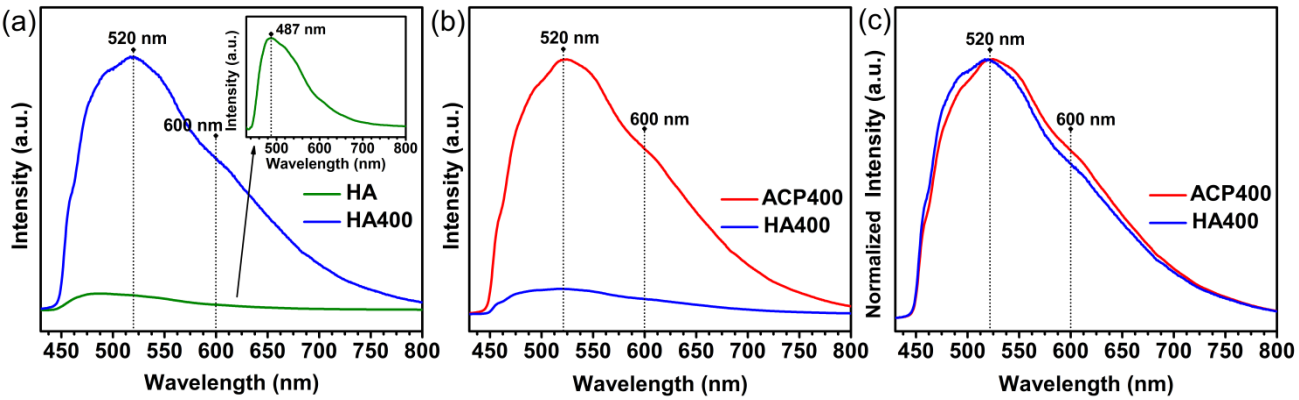

Figure 6. PL emission spectra (λ_{exc} = 405 nm) of (**a**) chemically precipitated HA obtained after ripening for 24 h and heat treatment at 400 ºC, and (**b,c**) PL spectra of ACP and HA heat-treated at 400 ºC, respectively.

In precipitated ACP NPs, perturbations in Ca and PO_4 electronic densities could occur as a result of fluctuations in Ca–O and P–O bond lengths and O–Ca–O and O–P–O bond angles (Figure 2), which are characteristic of the ACP structure, originating localized tail states (Figure 4). Besides, Bystrov et al. [55] evidenced by DFT calculations of HA that V_O vacancies in the PO_4 groups lead to fully occupied peaks at 344 nm (3.60 eV eV), 358 nm (3.47 eV), and 366 nm (3.39 eV) bellow the CB. Huerta et al. [41] experimentally proposed that this level occurs at 373 nm (3.32 eV). In this study, we propose that the defect-related excitation bands of ACP NPs centered at 370 nm (3.35 eV) and 398 nm

(3.10 eV) mainly stem from energy states associated with V_O in PO_4^{3-}. Therefore, the PL emission (Figure 5c) originates from excited electrons departing from this band, and subsequently follows a complex multistep decay through radiative and non-radiative pathways involving distinct extended and/or localized levels. These localized levels could arise from tail and defect states due to V_O in PO_4^{3-} and V_{Ca}, as well as from CO_3^{2-} impurity and defects associated with its stabilization in the ACP lattice.

The heat treatment of ACP at 400 ºC leads to a new excitation band in the 400-520 nm range, which is closer to the excitation wavelength used (450 nm), rendering improved PL emissions compared to the as-synthesized ACP NPs. We believe that this new band greatly contribute to temperature-induced changes in the CO_3^{2-} impurity trapped in ACP400 NPs and their environments. Zollfrank et al. [32] proposed that annealing biomimetic HA at 400 ºC enhances the presence of self-trapped electrons in carbonates (CO_3^{3-}), resulting in improved PL emission. Our recent studies [37,50] with HA corroborated the investigations conducted by Gonzalez et al. [40], who concluded that CO_3^{2-} impurities could play an important role in the PL emission observed in NPs heated at 350-450 ºC. In the case of the ACP structure, the SRO modifications in the CO_3^{2-} group observed by the FTIR spectrum of ACP400 NPs (Figure 2b) confirm the aforementioned arguments since (1) this group becomes richer in electronic density after annealing due to changes in interaction with the surrounding crystal field, and (2) the CO_3^{2-} environment becomes more anisotropic (i.e., greater C–O bond distortions). As a consequence, both the changes in bond character of the CO_3^{2-} group and in its surroundings and the pronounced impact of the short-range disorder on the CO_3^{2-} internal arrangement contribute to the improved excitation capability of ACP400 NPs in higher wavelength regions compared to ACP NPs.

Furthermore, Zhang et al. [35] related the role of $CO_2^{\bullet-}$ radicals to the PL observed in HA. More recently, Jiang et al. [97] observed that these impurities are in fact N-rich carbon dots present on the surface and inside HA NPs acting as luminescent centers, which was further corroborated by other

studies [51,54]. However, no clear signs of carbon dots were observed herein. The main difference is that these authors used significant amounts of citrate precursors, which are known to decompose into carbon dots by hydrothermal treatment. Even though we observed the presence of graphitized carbon adsorbed on the surface of ACP400 NPs by XPS (section 3.3), the substantial contribution of adventitious carbon to the PL emission can be discarded since it is known that a similar adsorption capability is retained on the NPs after ACP→HA transition [98]. Nevertheless, as shown in Figure 6b the emission intensity of the HA400 sample is 5 times less intense than that of ACP400 NPs.

Lattice water elimination when ACP is heat-treated up to 400 ºC is then a crucial mechanism to improve the PL properties of ACP400 NPs. Hydration water was previously proposed by Posner and Betts [63] to occupy interstitial positions between the $Ca_9(PO_4)_6$ clusters composing the ACP NPs. Termine and Lundy [66] argued that H_2O molecules contribute to the ACP coordination structure, while Du et al. [99] recently proposed that this water is coordinated with Ca atoms of the outer shell of Posner's subunits. Moreover, Uskoković et al. [62] stated that before annealing the water-rich ACP lattice possesses a large amount of hydrogen bonding between H_2O molecules and $PO^{3}_{4}^{-}$ groups.

Due to this active bonding between H_2O molecules and their surroundings, it could be expected that their removal influences the bond character of the remaining atomic groups in the ACP lattice, as observed for the strongly polarizable $PO^{3}_{4}^{-}$ and $CO^{2}_{3}^{-}$ groups. Additionally, as evidenced by Uskoković [61] an important shrinkage of the ACP lattice occurs by heating up to 400 ºC in order to close the voids resulting from water release. This contraction with consequent increase in lattice strain and decrease in SRO of the ACP400 lattice, observable as shifts and broadening of the bands related to $PO^{3}_{4}^{-}$ and $CO^{2}_{3}^{-}$ vibrational modes in FTIR (Figures 2d and 2f), could intensify the electronic interactions between neighboring atomic groups, causing a significant increase in the PL emission intensity. This can be attributed to the increment in the oscillator strength and the consequent higher probability of radiative electronic transitions, as well as the increase in the density of localized states within the forbidden zone.

In our previous publication [37], we also observed an important contraction in the crystalline lattice of HA NPs up to 400 ºC/4h after the elimination of impurities with consequent increase in PL emission. This difference in PL intensity between ACP400 and HA400 materials could be mainly related to the distinct characteristics of hydration water in their lattices. When the ACP→HA transition takes place in aqueous media, the concentration of hydration water is known to be reduced from ~15wt% for ACP to values below 3.5wt% for HA [50,65]. Additionally, the activation energy (E_a) for dehydration is also reduced from 23.6 kJ/mol for ACP to 12.5 kJ/mol^{-1} for HA [62]. Thereby, ACP has a higher concentration of hydration water molecules, which are more tightly bounded in its amorphous lattice than in HA. These characteristics imply a less pronounced structural impact at short range in the HA lattice than in ACP due to the loss of water, leading to a lower density of similar localized energy states and/or a reduced probability of radiative electronic transitions in HA400 NPs.

In summary, the experimental data obtained in this study evidenced that the heat treatment at intermediate temperatures close to 400 ºC is an important step to obtain CaPs with improved PL properties. The concomitant impurity reactions (H_2O and CO_3^{2-}) that take place in the ACP lattice during temperature-induced structural reorganization play a key role in this procedure. These results could bring insights into new optical devices using ACP400 NPs with stable structural and PL properties, as demonstrated by the stability analysis conducted after 10 months by FTIR and PL emission spectrum (Figure S4), where no significant changes were observed in comparison with the as-synthesized ACP400 sample.

3.8. Cytotoxicity assay

MTT assay was used to evaluate the cytotoxicity of ACP400 NPs on HDFn cells, and the results are shown in Figure 7. After incubation with ACP400 NPs for 24 and 48 h, the HDFn cell viability was superior to 95% in all tested concentrations (from 20 to 320 μg/mL). The statistical analysis revealed no significant difference between control and ACP400 NPs, except for the ones containing 20 μg/mL

(24 h), 40 and 80 μg/mL (48 h) of NPs, in which a slight increase in cell viability occurred. These results are in accordance with the superior cell viability found for luminescent HA NPs exposed to HDFn cells in similar conditions [50]. Therefore, the low cytotoxicity observed for the luminescent ACP400 NPs evidences the potential of this CaP to be used as a safe material for forensics purposes.

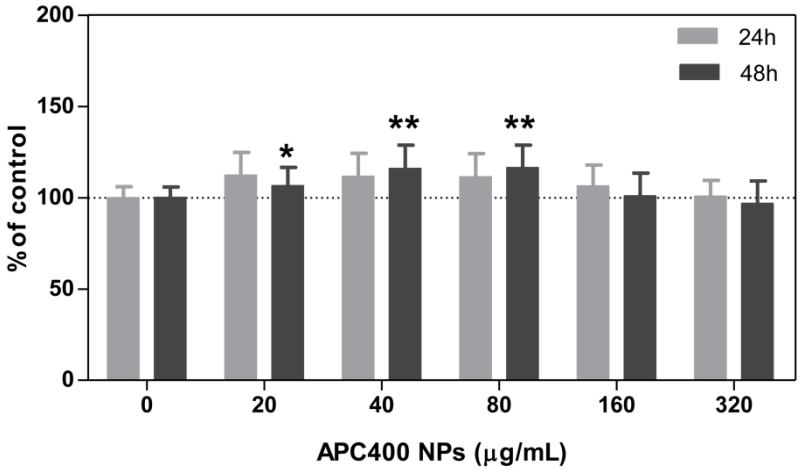

Figure 7. Cell viability analysis of HDFn cells after incubation with increasing concentrations of ACP400 NPs for 24 and 48 h. Mean ± SD of three independent experiments in triplicate. Asterisks indicate difference in comparison with the control (* $p<0.5$ and ** $p<0.01$).

3.9. Application for fingerprint imaging

The feasibility of ACP400 NPs for fingerprint imaging was probed in a pair of surfaces from utensils of daily use, and the results are shown in Figure 8. Under NUV light, the fingerprints were successfully detected by the pale fluorescent yellow color of ACP400 NPs. Moreover, a more accurate image was observed on stainless-steel tweezers (Figure 8a) than on the smart screen surface of the polymeric material (Figure 8d). This allowed us to obtain clear and well-resolved ridges, bifurcations, and lakes.

To evaluate the viability of AC400 NPs as an alternative system for latent fingerprint imaging, the digitalized images obtained from both stainless-steel tweezers (Figure 8b) and the polymeric material (Figure 8e) were compared with those from the police database collected by standard procedure (ink fingerprinting) (Figures 8c and 8f). After inserting the data into the Integrated Automated Fingerprint Identification System (IAFIS), we conducted a process using a computer to

match fingerprints against a database of known fingerprints. Our analysis compared the different traits in the obtained fingerprints, returning 14 matches. These results agree with the forensic requirements that must be taken in account for future legal actions.

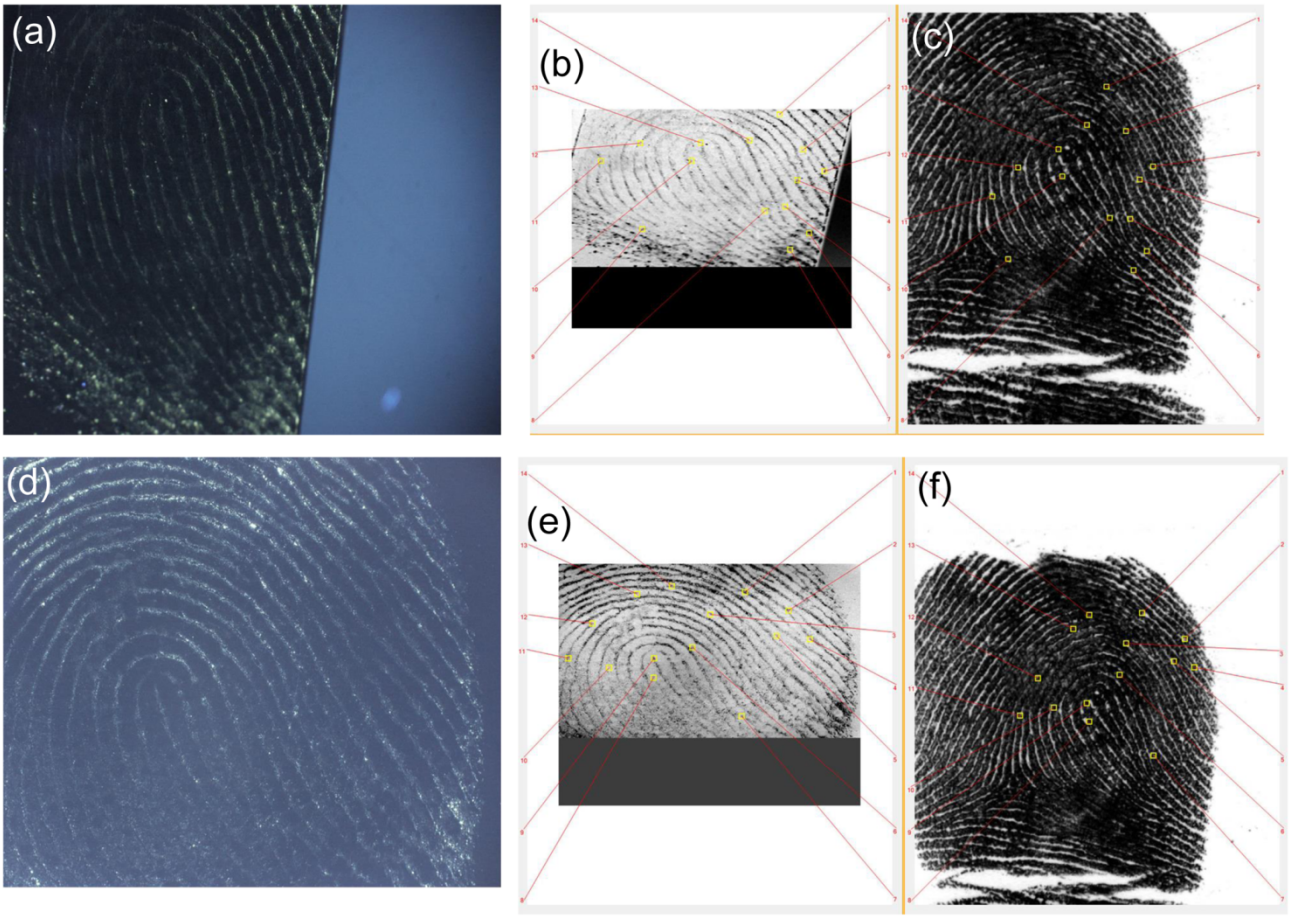

Figure 8. Latent fingerprint images based on ACP400 NPs obtained under NUV irradiation on (**a**) tweezers and (**b**) the LCD screen of a smartphone. (**c,d**) Digitalized images of UV exposed surfaces containing ACP400 NPs. (**e,f**) Digitalized images of fingerprints obtained from the standard procedure (ink fingerprinting). Data analysis was conducted using IAFIS system.

The mechanism for fingerprint imaging could be explained by electrostatic interactions of the negative surface due to O=P-O functional groups (mainly phosphate) and basic proteins of the secretion components, as previously reported [86]. The role of the analyst is to compare minutiae characteristics and locations and determine if they match. Our analysis showed the satisfactory performance of ACP400 when used for latent fingerprint detection. The produced ACP400 NPs are fluorescent and non-toxic, and the images obtained are more shinny than those obtained with ink.

4. Conclusions

In summary, intrinsically photoluminescent, biocompatible, and stable nanoparticles based on chemically precipitated ACP heat-treated at 400 ºC for 4 h were successfully synthesized. SAED and XRD results confirmed that the amorphous pattern was present after the heat treatment, and a significant decrease in the structural short-range order was detected in FTIR as a broadening of the $PO^{3}_{4}^{-}$ bands and as an increase in peak asymmetry. Furthermore, the stereochemistry of the structural $CO^{2}_{3}^{-}$ groups present within the ACP amorphous lattice was also significantly affected. These structural changes occurred due to the shrinkage of the ACP lattice as an effect of hydration water elimination at 400 ºC. The aforementioned phenomena, together with V_{Ca} and V_O vacancy in $PO^{3}_{4}^{-}$, were attributed to be the possible causes of the high density of localized tail and defect states inside the forbidden band gap of the heat-treated ACP, detected by diffuse reflectance via UV-Vis spectroscopy and by photoluminescence excitation and emission measurements.

When excited at λ_{exc} = 450 nm, the photoluminescence emission of the heat-treated ACP nanoparticles was found to be 50 times greater than the freshly precipitated ACP. Additionally, it consisted of a broadband defect-related emission profile centered at 540 nm, encompassing most part of the visible region (490-800 nm). The emission had a yellowish color, as determined by CIE chromaticity coordinates using distinct excitation sources (x = 0.53; y = 0.45, spectrofluorometer, and x = 0.52; y = 0.44, HeCd laser). The structural and luminescent features remained almost unchanged after 10 months, demonstrating the superior stability of the heat-treated nanoparticles. When used for fingerprint imaging, the unique bright yellow patterns of ACP luminescence were well observed on the surface of tweezers and the LCD screen of a smartphone under NUV irradiation (λ_{exc} = 450 nm). These nanoparticles presented interactions with biomolecules, leading to specific fluorescent patterns. Moreover, the non-cytotoxic response of ACP observed by MTT assay evidenced the potential of this calcium orthophosphate to be used as a safe material for forensics purposes.

Acknowledgments

The authors acknowledge the financial support of the following agencies: Conselho Nacional de Desenvolvimento Científico e Tecnológico (CNPq, Grants 164373/2020-9 and 141964/2018-9), Fundação de Amparo à Pesquisa do Estado de São Paulo (FAPESP, Grant 2013/07296-2), and COST Action 16101. Special Thanks to Prof. Andrea Simone Stucchi de Camargo Alvarez Bernardez and Dr. Leonnam Gotardo Merizio for the support with photoluminescence spectroscopy measurements and Prof. Waldir Avansi for the support with UV-Vis spectroscopy.

References

[1] D.R. Ashbaugh, Quantitative-qualitative friction ridge analysis: An introduction to basic and advanced ridgeology, CRC Press, Boca Raton, Florida, 1999.

[2] A.K. Jain, A. Ross, S. Prabhakar, An introduction to biometric recognition, IEEE Trans. Circuits Syst. Video Technol. 14 (2004) 4–20. https://doi.org/10.1109/TCSVT.2003.818349.

[3] D.A. Wilkinson, A. Misner, A comparison of thenoyl europium chelate with ardrox and rhodamine 6G for fluorescent detection of cyanoacrylate prints, J. Forensic Identif. 44 (1994) 387–407.

[4] G. Sodhi, J. Kaur, R.K. Garg, Fingerprint powder formulations based on organic, fluorescent dyes, J. Forensic Identif. 54 (2004) 4–8.

[5] D.S. Bhagat, P.B. Chavan, W.B. Gurnule, S.K. Shejul, I.V. Suryawanshi, Efficacy of synthesized azo dye for development of latent fingerprints on non-porous and wet surfaces, Mater. Today Proc. 29 (2020) 1223–1228. https://doi.org/10.1016/j.matpr.2020.05.480.

[6] H.L. Barros, L. Tavares, V. Stefani, Dye-doped starch microparticles as a novel fluorescent agent for the visualization of latent fingermarks on porous and non-porous substrates, Forensic Chem. 20 (2020) 100264. https://doi.org/10.1016/j.forc.2020.100264.

[7] M. Chen, R. Chen, Y. Shi, J. Wang, Y. Cheng, Y. Li, X. Gao, Y. Yan, J.Z. Sun, A. Qin, R.T.K. Kwok, J.W.Y. Lam, B.Z. Tang, Malonitrile-functionalized tetraphenylpyrazine: Aggregation-induced emission, ratiometric detection of hydrogen sulfide, and mechanochromism, Adv. Funct. Mater. 28 (2018) 1704689. https://doi.org/10.1002/adfm.201704689.

[8] C. Yuan, M. Li, M. Wang, X. Zhang, Z. Yin, K. Song, Z. Zhang, Sensitive development of latent fingerprints using Rhodamine B-diatomaceous earth composites and principle of efficient image enhancement behind their fluorescence characteristics, Chem. Eng. J. 383 (2020) 123076. https://doi.org/10.1016/j.cej.2019.123076.

[9] M.J. Choi, K.E. McBean, P.H.R. Ng, A.M. McDonagh, P.J. Maynard, C. Lennard, C. Roux, An evaluation of nanostructured zinc oxide as a fluorescent powder for fingerprint detection, J. Mater. Sci. 43 (2008) 732–737. https://doi.org/10.1007/s10853-007-2178-5.

[10] M. Algarra, J. Jiménez-Jiménez, R. Moreno-Tost, B.B. Campos, J.C.G. Esteves da Silva, CdS nanocomposites assembled in porous phosphate heterostructures for fingerprint detection, Opt. Mater. (Amst). 33 (2011) 893–898. https://doi.org/10.1016/j.optmat.2011.01.017.

[11] J. Dutta, S.A. Ramakrishna, I. Mekkaoui Alaoui, Fingerprint visualization enhancement by deposition of columnar thin films and fluorescent dye treatment, Forensic Sci. Int. 228 (2013)

32–37. https://doi.org/10.1016/j.forsciint.2013.02.018.

[12] M. Algarra, K. Radotić, A. Kalauzi, D. Mutavdžić, A. Savić, J. Jiménez-Jiménez, E. Rodríguez-Castellón, J.C.G.E. da Silva, J.J. Guerrero-González, Fingerprint detection and using intercalated CdSe nanoparticles on non-porous surfaces, Anal. Chim. Acta. 812 (2014) 228–235. https://doi.org/10.1016/j.aca.2014.01.015.

[13] P. Wu, C. Xu, X. Hou, J.-J. Xu, H.-Y. Chen, Dual-emitting quantum dot nanohybrid for imaging of latent fingerprints: simultaneous identification of individuals and traffic light-type visualization of TNT, Chem. Sci. 6 (2015) 4445–4450. https://doi.org/10.1039/C5SC01497B.

[14] K. Cai, R. Yang, Y. Wang, X. Yu, J. Liu, Super fast detection of latent fingerprints with water soluble CdTe quantum dots, Forensic Sci. Int. 226 (2013) 240–243. https://doi.org/10.1016/j.forsciint.2013.01.035.

[15] J. Liu, Z. Shi, Y. Yu, R. Yang, S. Zuo, Water-soluble multicolored fluorescent CdTe quantum dots: Synthesis and application for fingerprint developing, J. Colloid Interface Sci. 342 (2010) 278–282. https://doi.org/10.1016/j.jcis.2009.10.061.

[16] M. Wang, M. Li, A. Yu, J. Wu, C. Mao, Rare earth fluorescent nanomaterials for enhanced development of latent fingerprints, ACS Appl. Mater. Interfaces. 7 (2015) 28110–28115. https://doi.org/10.1021/acsami.5b09320.

[17] N.M. Maalej, A. Qurashi, I. Bennour, L.R. Haddada, M.N. Shaikh, M. Ilyas, N. Essoukri Ben Amara, R. Maalej, M.A. Gondal, Green emitting rare earth Gd_2O_3:Tb^{3+} nanoparticles for rapid imaging of latent fingerprint, Methods Appl. Fluoresc. 9 (2021) 025002. https://doi.org/10.1088/2050-6120/abdbc0.

[18] X. Wang, L. Yan, S. Liu, P. Zhang, R. Huang, B. Zhou, Enhancing energy migration upconversion through a migratory interlayer in the core–shell–shell nanostructure towards latent fingerprinting, Nanoscale. 12 (2020) 18807–18814. https://doi.org/10.1039/D0NR03817B.

[19] Y. Yang, X. Liu, Y. Lu, L. Tang, J. Zhang, L. Ge, F. Li, Visualization of latent fingerprints using a simple "silver imaging ink," Anal. Methods. 8 (2016) 6293–6297. https://doi.org/10.1039/C6AY01811D.

[20] Y. Wang, Y. Xue, J. Wang, Y. Zhu, X. Wang, X. Zhang, Y. Zhu, J. Liao, X. Li, X. Wu, W. Chen, Biocompatible and photoluminescent carbon dots/hydroxyapatite/PVA dual-network composite hydrogel scaffold and their properties, J. Polym. Res. 26 (2019) 6–11. https://doi.org/10.1007/s10965-019-1907-1.

[21] Y.-H. Cheng, Y. Zhang, S.-L. Chau, S.K.-M. Lai, H.-W. Tang, K.-M. Ng, Enhancement of image contrast, stability, and SALDI-MS detection sensitivity for latent fingerprint analysis by tuning the composition of silver–gold nanoalloys, ACS Appl. Mater. Interfaces. 8 (2016) 29668–29675. https://doi.org/10.1021/acsami.6b09668.

[22] G. Kolhatkar, C. Parisien, A. Ruediger, C. Muehlethaler, Latent fingermark imaging by single-metal deposition of gold nanoparticles and surface enhanced raman spectroscopy, Front. Chem. 7 (2019) 440. https://doi.org/10.3389/fchem.2019.00440.

[23] I. Milenkovic, M. Algarra, C. Alcoholado, M. Cifuentes, J.M. Lázaro-Martínez, E. Rodríguez-Castellón, D. Mutavdžić, K. Radotić, T.J. Bandosz, Fingerprint imaging using N-doped carbon dots, Carbon N. Y. 144 (2019) 791–797. https://doi.org/10.1016/j.carbon.2018.12.102.

[24] D. Fernandes, M.J. Krysmann, A. Kelarakis, Carbogenically coated silica nanoparticles and their forensic applications, Chem. Commun. 52 (2016) 8294–8296. https://doi.org/10.1039/C6CC02556K.

[25] M. Algarra, D. Bartolić, K. Radotić, D. Mutavdžić, M.S. Pino-González, E. Rodríguez-Castellón, J.M. Lázaro-Martínez, J.J. Guerrero-González, J.C. Esteves da Silva, J. Jiménez-Jiménez, P-doped carbon nano-powders for fingerprint imaging, Talanta. 194 (2019) 150–157.

https://doi.org/10.1016/j.talanta.2018.10.033.

[26] E. Prabakaran, K. Pillay, Synthesis and characterization of fluorescent N-CDs/ZnONPs nanocomposite for latent fingerprint detection by using powder brushing method, Arab. J. Chem. 13 (2020) 3817–3835. https://doi.org/10.1016/j.arabjc.2019.01.004.

[27] F. Wang, W.B. Tan, Y. Zhang, X. Fan, M. Wang, Luminescent nanomaterials for biological labelling, Nanotechnology. 17 (2006) R1–R13. https://doi.org/10.1088/0957-4484/17/1/R01.

[28] M. Vallet-Regí, J.M. González-Calbet, Calcium phosphates as substitution of bone tissues, Prog. Solid State Chem. 32 (2004) 1–31. https://doi.org/10.1016/j.progsolidstchem.2004.07.001.

[29] K. Lin, C. Wu, J. Chang, Advances in synthesis of calcium phosphate crystals with controlled size and shape, Acta Biomater. 10 (2014) 4071–4102. https://doi.org/10.1016/j.actbio.2014.06.017.

[30] C. Qi, J. Lin, L.H. Fu, P. Huang, Calcium-based biomaterials for diagnosis, treatment, and theranostics, Chem. Soc. Rev. 47 (2018) 357–403. https://doi.org/10.1039/c6cs00746e.

[31] S.S. Syamchand, G. Sony, Multifunctional hydroxyapatite nanoparticles for drug delivery and multimodal molecular imaging, Microchim. Acta. 182 (2015) 1567–1589. https://doi.org/10.1007/s00604-015-1504-x.

[32] C. Zollfrank, L. Müller, P. Greil, F.A. Müller, Photoluminescence of annealed biomimetic apatites, Acta Biomater. 1 (2005) 663–669. https://doi.org/10.1016/j.actbio.2005.06.004.

[33] D. Aronov, A. Karlov, G. Rosenman, Hydroxyapatite nanoceramics: Basic physical properties and biointerface modification, J. Eur. Ceram. Soc. 27 (2007) 4181–4186. https://doi.org/10.1016/j.jeurceramsoc.2007.02.121.

[34] D. Aronov, M. Chaikina, J. Haddad, A. Karlov, G. Mezinskis, L. Oster, I. Pavlovska, G. Rosenman, Electronic states spectroscopy of Hydroxyapatite ceramics, J. Mater. Sci. Mater. Med. 18 (2007) 865–870. https://doi.org/10.1007/s10856-006-0080-3.

[35] C. Zhang, J. Yang, Z. Quan, P. Yang, C. Li, Z. Hou, J. Lin, Hydroxyapatite nano- and microcrystals with multiform morphologies: Controllable synthesis and luminescence properties, Cryst. Growth Des. 9 (2009) 2725–2733. https://doi.org/10.1021/cg801353n.

[36] A. V. Bystrova, Y.D. Dekhtyar, A.I. Popov, J. Coutinho, V.S. Bystrov, Modified hydroxyapatite structure and properties: Modeling and synchrotron data analysis of modified hydroxyapatite structure, Ferroelectrics. 475 (2015) 135–147. https://doi.org/10.1080/00150193.2015.995580.

[37] T.R. Machado, J.C. Sczancoski, H. Beltrán-Mir, I.C. Nogueira, M.S. Li, J. Andrés, E. Cordoncillo, E. Longo, A novel approach to obtain highly intense self-activated photoluminescence emissions in hydroxyapatite nanoparticles, J. Solid State Chem. 249 (2017) 64–69. https://doi.org/10.1016/j.jssc.2016.12.018.

[38] T.R. Machado, J.C. Sczancoski, H. Beltrán-Mir, M.S. Li, J. Andrés, E. Cordoncillo, E. Leite, E. Longo, Structural properties and self-activated photoluminescence emissions in hydroxyapatite with distinct particle shapes, Ceram. Int. 44 (2018) 236–245. https://doi.org/10.1016/j.ceramint.2017.09.164.

[39] D.L. Goloshchapov, P. V. Seredin, D.A. Minakov, E.P. Domashevskaya, Photoluminescence Properties of Nanoporous Nanocrystalline Carbonate-Substituted Hydroxyapatite, Opt. Spectrosc. (English Transl. Opt. i Spektrosk). 124 (2018) 187–192. https://doi.org/10.1134/S0030400X18020066.

[40] G. Gonzalez, C. Costa-Vera, L.J. Borrero, D. Soto, L. Lozada, J.I. Chango, J.C. Diaz, L. Lascano, Effect of carbonates on hydroxyapatite self-activated photoluminescence response, J. Lumin. 195 (2018) 385–395. https://doi.org/10.1016/j.jlumin.2017.11.058.

[41] V.J. Huerta, P. Fernández, V. Gómez, O.A. Graeve, M. Herrera, Defect-related luminescence

properties of hydroxyapatite nanobelts, Appl. Mater. Today. 21 (2020) 100822. https://doi.org/10.1016/j.apmt.2020.100822.

[42] E.X. Figueroa-Rosales, J. Martínez-Juárez, E. García-Díaz, D. Hernández-Cruz, S.A. Sabinas-Hernández, M.J. Robles-Águila, Photoluminescent properties of hydroxyapatite and hydroxyapatite/multi-walled carbon nanotube composites, Crystals. 11 (2021) 832. https://doi.org/10.3390/cryst11070832.

[43] A. Sinha, A. Pal, A.S.S. Murmu, U.K.G. Amit, R. Chowdhury, Calcination Temperature-Dependent Structural and Photoluminescence Properties of Hydroxyapatite Derived from Labeo Rohita Fish Scales, J. Inst. Eng. Ser. D. (2020). https://doi.org/10.1007/s40033-020-00232-3.

[44] C. Zhang, C. Li, S. Huang, Z. Hou, Z. Cheng, P. Yang, C. Peng, J. Lin, Self-activated luminescent and mesoporous strontium hydroxyapatite nanorods for drug delivery, Biomaterials. 31 (2010) 3374–3383. https://doi.org/10.1016/j.biomaterials.2010.01.044.

[45] Z. Li, Z. Liu, M. Yin, X. Yang, Q. Yuan, J. Ren, X. Qu, Aptamer-capped multifunctional mesoporous strontium hydroxyapatite nanovehicle for cancer-cell-responsive drug delivery and imaging, Biomacromolecules. 13 (2012) 4257–4263. https://doi.org/10.1021/bm301563q.

[46] G.S. Kumar, E.K. Girija, Flower-like hydroxyapatite nanostructure obtained from eggshell: A candidate for biomedical applications, Ceram. Int. 39 (2013) 8293–8299. https://doi.org/10.1016/j.ceramint.2013.03.099.

[47] R.K. Singh, T.H. Kim, K.D. Patel, J.J. Kim, H.W. Kim, Development of biocompatible apatite nanorod-based drug-delivery system with in situ fluorescence imaging capacity, J. Mater. Chem. B. 2 (2014) 2039–2050. https://doi.org/10.1039/c3tb21156h.

[48] S.Y. Park, K. Il Kim, S.P. Park, J.H. Lee, H.S. Jung, Aspartic Acid-Assisted Synthesis of Multifunctional Strontium-Substituted Hydroxyapatite Microspheres, Cryst. Growth Des. 16 (2016) 4318–4326. https://doi.org/10.1021/acs.cgd.6b00420.

[49] K. Deshmukh, M.M. Shaik, S.R. Ramanan, M. Kowshik, Self-Activated Fluorescent Hydroxyapatite Nanoparticles: A Promising Agent for Bioimaging and Biolabeling, ACS Biomater. Sci. Eng. 2 (2016) 1257–1264. https://doi.org/10.1021/acsbiomaterials.6b00169.

[50] T.R. Machado, I.S. Leite, N.M. Inada, M.S. Li, J.S. da Silva, J. Andrés, H. Beltrán-Mir, E. Cordoncillo, E. Longo, Designing biocompatible and multicolor fluorescent hydroxyapatite nanoparticles for cell-imaging applications, Mater. Today Chem. 14 (2019) 100211. https://doi.org/10.1016/j.mtchem.2019.100211.

[51] C. Wang, K.-J. Jeong, J. Kim, S.W. Kang, J. Kang, I.H. Han, I.-W. Lee, S.-J. Oh, J. Lee, Emission-tunable probes using terbium(III)-doped self-activated luminescent hydroxyapatite for in vitro bioimaging, J. Colloid Interface Sci. 581 (2021) 21–30. https://doi.org/10.1016/j.jcis.2020.07.083.

[52] K. Zhang, K. Zeng, C. Shen, S. Tian, M. Yang, Determination of protein kinase A activity and inhibition by using hydroxyapatite nanoparticles as a fluorescent probe, Microchim. Acta. 185 (2018). https://doi.org/10.1007/s00604-018-2754-1.

[53] W. Yang, J. Luo, M. Qi, M. Yang, Detection of alkaline phosphatase activity and inhibition with fluorescent hydroxyapatite nanoparticles, Anal. Methods. 11 (2019) 2272–2276. https://doi.org/10.1039/c9ay00176j.

[54] C. Cheng, K. Tong, Y. Fang, J. Wang, Y. Liu, J. Tan, Ammonium-induced synthesis of highly fluorescent hydroxyapatite nanoparticles with excellent aqueous colloidal stability for secure information storage, Coatings. 9 (2019) 1–14. https://doi.org/10.3390/coatings9050289.

[55] V.S. Bystrov, C. Piccirillo, D.M. Tobaldi, P.M.L. Castro, J. Coutinho, S. Kopyl, R.C. Pullar, Oxygen vacancies, the optical band gap (Eg) and photocatalysis of hydroxyapatite: Comparing

modelling with measured data, Appl. Catal. B Environ. 196 (2016) 100–107. https://doi.org/10.1016/j.apcatb.2016.05.014.

[56] G. Lambrecht, C. Mallol, Autofluorescence of experimentally heated bone: Potential archaeological applications and relevance for estimating degree of burning, J. Archaeol. Sci. Reports. 31 (2020) 102333. https://doi.org/10.1016/j.jasrep.2020.102333.

[57] A. Sandri, P.R. Basso, I. Corridori, M. Protasoni, G. Segalla, M. Raspanti, A.E. Spinelli, F. Boschi, Photon emission and changes in fluorescent properties of bone after laser irradiation, J. Biophotonics. 14 (2021) 1–9. https://doi.org/10.1002/jbio.202000445.

[58] D.L. Goloshchapov, D.A. Minakov, E.P. Domashevskaya, P. V. Seredin, Excitation of luminescence of the nanoporous bioactive nanocrystalline carbonate-substituted hydroxyapatite for early tooth disease detection, Results Phys. 7 (2017) 3853–3858. https://doi.org/10.1016/j.rinp.2017.09.055.

[59] S. V. Dorozhkin, Amorphous calcium (ortho)phosphates, Acta Biomater. 6 (2010) 4457–4475. https://doi.org/10.1016/j.actbio.2010.06.031.

[60] C. Combes, C. Rey, Amorphous calcium phosphates: Synthesis, properties and uses in biomaterials, Acta Biomater. 6 (2010) 3362–3378. https://doi.org/10.1016/j.actbio.2010.02.017.

[61] V. Uskoković, Disordering the disorder as the route to a higher order: incoherent crystallization of calcium phosphate through amorphous precursors, Cryst. Growth Des. 19 (2019) 4340–4357. https://doi.org/10.1021/acs.cgd.9b00061.

[62] V. Uskoković, S. Marković, L. Veselinović, S. Škapin, N. Ignjatović, D.P. Uskoković, Insights into the kinetics of thermally induced crystallization of amorphous calcium phosphate, Phys. Chem. Chem. Phys. 20 (2018) 29221–29235. https://doi.org/10.1039/c8cp06460a.

[63] A.S. Posner, F. Betts, Synthetic amorphous calcium phosphate and its relation to bone mineral structure, Acc. Chem. Res. 8 (1975) 273–281.

[64] S. Somrani, M. Banu, M. Jemal, C. Rey, Physico-chemical and thermochemical studies of the hydrolytic conversion of amorphous tricalcium phosphate into apatite, J. Solid State Chem. 178 (2005) 1337–1348. https://doi.org/10.1016/j.jssc.2004.11.029.

[65] E.D. Eanes, Thermochemical studies on amorphous calcium phosphate, Calcif. Tissue Res. 5 (1970) 133–145. https://doi.org/10.1007/BF02017543.

[66] J.D. Termine, D.R. Lundy, Vibrational spectra of some phosphate salts amorphous to X-ray diffraction, Calcif. Tissue Res. 15 (1974) 55–70. https://doi.org/10.1007/BF02059043.

[67] S.J. Gadaleta, E.P. Paschalis, F. Betts, R. Mendelsohn, A.L. Boskey, Fourier transform infrared spectroscopy of the solution-mediated conversion of amorphous calcium phosphate to hydroxyapatite: New correlations between X-ray diffraction and infrared data, Calcif. Tissue Int. 58 (1996) 9–16. https://doi.org/10.1007/BF02509540.

[68] D. Tadic, F. Peters, M. Epple, Continuous synthesis of amorphous carbonated apatites, Biomaterials. 23 (2002) 2553–2559. https://doi.org/10.1016/S0142-9612(01)00390-8.

[69] J. Vecstaudza, M. Gasik, J. Locs, Amorphous calcium phosphate materials: Formation, structure and thermal behaviour, J. Eur. Ceram. Soc. 39 (2019) 1642–1649. https://doi.org/10.1016/j.jeurceramsoc.2018.11.003.

[70] P.C.H. Mitchell, S.F. Parker, K. Simkiss, J. Simmons, M.G. Taylor, Hydrated sites in biogenic amorphous calcium phosphates: An infrared, Raman, and inelastic neutron scattering study, J. Inorg. Biochem. 62 (1996) 183–197. https://doi.org/10.1016/0162-0134(95)00146-8.

[71] J.M. Holmes, R.A. Beebe, Surface areas by gas adsorption on amorphous calcium phosphate and crystalline hydroxyapatite, Calcif. Tissue Res. 7 (1971) 163–174. https://doi.org/10.1007/BF02062604.

[72] M. Fleet, Carbonated hydroxyapatite: Materials, synthesis, and applications, Pan Stanford Publishing, New York, 2015.

[73] T. Theophanides, Infrared spectroscopy - Materials Science, Engineering and Technology, InTech, Rijeka, 2012.

[74] D. Stoilova, V. Koleva, V. Vassileva, Infrared study of some synthetic phases of malachite ($Cu_2(OH)_2CO_3$)-hydrozincite ($Zn_5(OH)_6(CO_3)_2$) series, Spectrochim. Acta - Part A Mol. Biomol. Spectrosc. 58 (2002) 2051–2059. https://doi.org/10.1016/S1386-1425(01)00677-1.

[75] J.E. Amonette, D. Rai, Identification of noncrystalline $(Fe,Cr)(OH)_3$ by infrared spectroscopy, Clays Clay Miner. 38 (1990) 129–136.

[76] J.P. Jolivet, Y. Thomas, B. Taravel, V. Lorenzelli, G. Busca, Infrared spectra of cerium and thorium pentacarbonate complexes, J. Mol. Struct. 79 (1982) 403–408. https://doi.org/10.1016/0022-2860(82)85091-6.

[77] J.F. Moulder, W.F. Stickle, P.E. Sobol, K.D. Bomben, Handbook of X-ray photoelectron spectroscopy: A reference book of standard spectra for identification and interpretation of XPS Data, Perkin-Elmer Corporation, Physical Electronics, Minnesota, 1995.

[78] V. Bemmer, M. Bowker, J.H. Carter, P.R. Davies, L.E. Edwards, K.D.M. Harris, C.E. Hughes, F. Robinson, D.J. Morgan, M.G. Thomas, Rationalization of the X-ray photoelectron spectroscopy of aluminium phosphates synthesized from different precursors, RSC Adv. 10 (2020) 8444–8452.

[79] S. Kasap, P. Capper, Springer handbook of electronic and photonic materials, 2nd edition, Springer International Publishing, Gewerbestrasse, Switzerland, 2017. https://doi.org/10.1007/978-3-319-48933-9_39.

[80] Z. Chen, H.N. Dinh, E. Miller, Photoelectrochemical Water Splitting: Standards, Experimental Methodos, and Protocols, Springer-Verlag, New York, 2013. https://doi.org/10.1016/B978-0-12-814134-2.00028-0.

[81] P. Makuła, M. Pacia, W. Macyk, How to correctly determine the band gap energy of modified semiconductor photocatalysts based on UV-Vis spectra, J. Phys. Chem. Lett. 9 (2018) 6814–6817. https://doi.org/10.1021/acs.jpclett.8b02892.

[82] L. Liang, P. Rulis, W.Y. Ching, Mechanical properties, electronic structure and bonding of α- and β-tricalcium phosphates with surface characterization, Acta Biomater. 6 (2010) 3763–3771. https://doi.org/10.1016/j.actbio.2010.03.033.

[83] P. Rulis, L. Ouyang, W.Y. Ching, Electronic structure and bonding in calcium apatite crystals: Hydroxyapatite, fluorapatite, chlorapatite, and bromapatite, Phys. Rev. B - Condens. Matter Mater. Phys. 70 (2004) 1–8. https://doi.org/10.1103/PhysRevB.70.155104.

[84] A. Slepko, A.A. Demkov, First-principles study of the biomineral hydroxyapatite, Phys. Rev. B - Condens. Matter Mater. Phys. 84 (2011) 1–11. https://doi.org/10.1103/PhysRevB.84.134108.

[85] M.E. Zilm, L. Chen, V. Sharma, A. McDannald, M. Jain, R. Ramprasad, M. Wei, Hydroxyapatite substituted by transition metals: Experiment and theory, Phys. Chem. Chem. Phys. 18 (2016) 16457–16465. https://doi.org/10.1039/c6cp00474a.

[86] Y. Jiménez-Flores, M. Suárez-Quezada, J.B. Rojas-Trigos, L. Lartundo-Rojas, V. Suárez, A. Mantilla, Characterization of Tb-doped hydroxyapatite for biomedical applications: optical properties and energy band gap determination, J. Mater. Sci. 52 (2017) 9990–10000. https://doi.org/10.1007/s10853-017-1201-8.

[87] N.L. Ignjatović, L. Mančić, M. Vuković, Z. Stojanović, M.G. Nikolić, S. Škapin, S. Jovanović, L. Veselinović, V. Uskoković, S. Lazić, S. Marković, M.M. Lazarević, D.P. Uskoković, Rare-earth (Gd^{3+},Yb^{3+}/Tm^{3+}, Eu^{3+}) co-doped hydroxyapatite as magnetic, up-conversion and down-

conversion materials for multimodal imaging, Sci. Rep. 9 (2019) 1–15. https://doi.org/10.1038/s41598-019-52885-0.

[88] S.S. Bhat, U. V. Waghmare, U. Ramamurty, First-principles study of structure, vibrational, and elastic properties of stoichiometric and calcium-deficient hydroxyapatite, Cryst. Growth Des. 14 (2014) 3131–3141. https://doi.org/10.1021/cg5004269.

[89] B. Goswami, A. Choudhury, Enhanced visible luminescence and modification in morphological properties of cadmium oxide nanoparticles induced by annealing, J. Exp. Nanosci. 10 (2015) 900–910. https://doi.org/10.1080/17458080.2014.933492.

[90] E. Cerrato, M.C. Paganini, E. Giamello, Photoactivity under visible light of defective ZnO investigated by EPR spectroscopy and photoluminescence, J. Photochem. Photobiol. A Chem. 397 (2020) 112531. https://doi.org/10.1016/j.jphotochem.2020.112531.

[91] V. Uskoković, D.P. Uskoković, Nanosized hydroxyapatite and other calcium phosphates: Chemistry of formation and application as drug and gene delivery agents, J. Biomed. Mater. Res. - Part B Appl. Biomater. 96 B (2011) 152–191. https://doi.org/10.1002/jbm.b.31746.

[92] G. Montes-Hernandez, F. Renard, Nucleation of brushite and hydroxyapatite from amorphous calcium phosphate phases revealed by dynamic in situ raman spectroscopy, J. Phys. Chem. C. 124 (2020) 15302–15311. https://doi.org/10.1021/acs.jpcc.0c04028.

[93] K. Onuma, A. Ito, Cluster growth model for hydroxyapatite, Chem. Mater. 10 (1998) 3346–3351. https://doi.org/10.1021/cm980062c.

[94] A. Lotsari, A.K. Rajasekharan, M. Halvarsson, M. Andersson, Transformation of amorphous calcium phosphate to bone-like apatite, Nat. Commun. 9 (2018) 4170. https://doi.org/10.1038/s41467-018-06570-x.

[95] K. Matsunaga, A. Kuwabara, First-principles study of vacancy formation in hydroxyapatite, Phys. Rev. B - Condens. Matter Mater. Phys. 75 (2007) 1–9. https://doi.org/10.1103/PhysRevB.75.014102.

[96] V.S. Bystrov, J. Coutinho, A. V. Bystrova, Y.D. Dekhtyar, R.C. Pullar, A. Poronin, E. Palcevskis, A. Dindune, B. Alkan, C. Durucan, E. V. Paramonova, Computational study of hydroxyapatite structures, properties and defects, J. Phys. D. Appl. Phys. 48 (2015) 195302. https://doi.org/10.1088/0022-3727/48/19/195302.

[97] D. Jiang, H. Zhao, Y. Yang, Y. Zhu, X. Chen, J. Sun, K. Yu, H. Fan, X. Zhang, Investigation of luminescent mechanism: N-rich carbon dots as luminescence centers in fluorescent hydroxyapatite prepared using a typical hydrothermal process, J. Mater. Chem. B. 5 (2017) 3749–3757. https://doi.org/10.1039/c6tb03184f.

[98] V. Uskoković, X-ray photoelectron and ion scattering spectroscopic surface analyses of amorphous and crystalline calcium phosphate nanoparticles with different chemical histories, Phys. Chem. Chem. Phys. 22 (2020) 5531–5547. https://doi.org/10.1039/c9cp06529f.

[99] L.W. Du, S. Bian, B. Di Gou, Y. Jiang, J. Huang, Y.X. Gao, Y.D. Zhao, W. Wen, T.L. Zhang, K. Wang, Structure of clusters and formation of amorphous calcium phosphate and hydroxyapatite: From the perspective of coordination chemistry, Cryst. Growth Des. 13 (2013) 3103–3109. https://doi.org/10.1021/cg400498j.